SAND2026-17757J

Investigation of O(^{3}P) Initiated Oxidation Products of 2,3-Dimethylfuran Using Synchrotron Photoionization

Yilan Lori Chen,[†(a)] Craig A. Taatjes,[b] and Giovanni Meloni[*(a,c)]

(a) Y.L. Chen, Dr. G. Meloni

Department of Chemistry, University of San Francisco, San Francisco, CA 94117 USA
E-mail: ylchen2@dons.usfca.edu

(b) Dr. C.A. Taatjes

Combustion Research Facility, Sandia National Laboratories, Livermore, CA 94550 USA
E-mail: cataatj@sandia.gov

(c) Dr. G. Meloni

Department of Biological and Chemical Sciences, New York Institute of Technology, Old Westbury, NY 11568 USA
E-mail: gmeloni@nyit.edu

KEYWORDS: photoionization mass spectrometry • synchrotron radiation • absolute photoionization cross-section • CBS-QB3 • combustion chemistry

ABSTRACT: Biofuels are an appealing alternative to augment conventional fossil fuels, given that traditional fossil fuels are finite in nature despite being the highest-consumed energy source. Furans have been studied as potential biofuels due to their renewability, high energy density, and ability to both blend with existing fossil fuels and serve as a stand-alone fuel. Although promising, more research efforts on the combustion of furan-based biofuels are needed. In this study, the oxidation of 2,3-dimethylfuran (2,3-DMF) initiated by O(^{3}P) was investigated using vacuum-ultraviolet synchrotron radiation from the Advanced Light Source at Lawrence Berkeley National Laboratory. The reaction was studied at 550 K and 7 torr. Major reaction products include 3-methyl-3-buten-2-one, 4,5-dimethyl-3(2H)-furanone, and 3-methyl-4-oxo-2(Z)-pentenal, with 3-methyl-3-buten-2-one being the most abundant.

INTRODUCTION

Fossil fuels have historically been the dominant energy source globally due to the use of coal, oil, and natural gas for electricity generation, heating, transportation, and other industrial processes.[1] However, combustion byproducts are a leading source of air pollutants such as volatile organic compounds (VOCs), nitrogen oxides (NO_x), carbon monoxide (CO), and particulate matter (PM).[2] Biofuel combustion has the possibility to reduce some of these pollutant emissions, and increasing biofuel use can be a means for a transition towards cleaner and more sustainable fuel blends as well as adding new energy capacity beyond fossil fuels.[3]

Biofuels are derived from organic materials, and their fuel blends can be used without requiring significant changes to infrastructure. They are characterized into three generations based on their production methods and sources. First-generation biofuels are sourced from food crops and vegetable oils like sugarcane and palm oil.[4] The production process involves fermentation or transesterification, converting the sugars from crops or the oils extracted from them into biofuels, such as ethanol or biodiesel.[5] Second generation biofuels utilize non-food crops and woody biomass as feedstocks, such as agricultural waste and silvergrass.[5] Its production process involves a more advanced pre-fermentation process, such as cellulosic production, to break down complex plant materials.[6] The production of third-generation biofuels entails cultivating microorganisms in controlled environments to optimize the generation of biofuel precursors, e.g., growing microalgae in a photobioreactor to produce lipids.[7]

Furan-based biofuels fall under second-generation biofuels, and a promising biofuel candidate includes 2,5-dimethylfuran (2,5-DMF), a structural isomer of 2,3-dimethylfuran. 2,5-DMF has a high volumetric density (31.5 MJ L^{-1}) and a high octane number (119), reducing engine knocking and increasing fuel efficiency.[8,9] The synthesis of hydroxymethylfurfural (HMF) from lignocelluosic biomass provides a >95% yield of 2,5-DMF derived from fructose.[10,11] Mixtures of 2,5-DMF with diesel (40% 2,5-DMF by volume) reduces soot emissions drastically compared to basic diesel in a single cylinder diesel

engine.[12] However, oxidation reactions of 2,3-DMF have not been extensively studied, and there is insufficient data available to compare reactivities to 2,5-DMF. Additionally, further research on radical additions to the double bond in furans and furan derivatives is required to draw details about elementary reactions initiated by radicals.[13] This work provides oxidation reaction data of 2,3-DMF initiated by ground state atomic oxygen, O(^{3}P), a prevalent radical found in combustion engines, to build upon previous research performed on the oxidation of 2,5-dimethylfuran with O(^{3}P).[8]

METHODS

Apparatus

The experiment was carried out in the Chemical Dynamics Beamline 9.0.2 at the Advanced Light Source (ALS) of Lawrence Berkeley National Laboratory using multiplexed time- and energy-resolved mass spectrometry coupled with tunable synchrotron radiation, which was used for the photoionization of reaction species.[14] The experimental setup is briefly covered here, and additional information regarding the experimental design is referenced elsewhere.[15–17] 2,3-dimethylfuran (Sigma-Aldrich, purity ≥ 99%) was purified via the freeze-pump-thaw technique, and its vapors were collected in a gas cylinder to reach a 0.37% mixture with helium (10.82 Torr 2,3-DMF in 2905 Torr He). The 0.37% mixture along with NO_2 was flowed into the reaction cell, then effused through a 650 μm wide pinhole on the side of the reactor into a differentially pumped ionization region, and the reaction was carried out at 550 K and 7 Torr. The concentration of NO_2 was calculated to be 7.37×10^{14} cm^{-3}, and the concentration of 2,3-DMF was approximately 4.58×10^{12} cm^{-3}. The pressure inside the reactor was kept constant by gas removal using a closed-loop feedback throttle valve via a capacitive manometer. The reactor temperature was adjusted using 18 μm thick resistive nichrome heating tape wrapped around the reactor tube. The photolysis of NO_2 generated O(^{3}P) using a 4 Hz pulsed unfocused XeF excimer laser at a wavelength of 351 nm. Based on the reported quantum yield of 1.00 for O(^{3}P) at 351 nm and the NO_2 absorption cross-section of 4.62×10^{-19} cm^2/molecule, the O(^{3}P) concentration was calculated to be 2.02×10^{12} cm^{-3}.[18,19] The ionized reaction species were then accelerated, collimated, and detected by a 50 kHz pulsed orthogonal time-of-flight mass spectrometer. Products were characterized by analyzing a three-dimensional data block containing mass-to-charge ratio (m/z), reaction time (ms), photon energy (eV), and relative ion signal.

To obtain the absolute photoionization cross section of 2,3-DMF, calibrated mass flow controllers were used to introduce known amounts of helium gas, the molecule of interest, and the calibration gas mixture comprising of ethene, propene, and 1-butene into the reaction tube. For this measurement the 62-cm quartz slow flow reactor was held at a constant pressure of 4 Torr, 298 K, and total flow of 100 sccm.

Measurement Procedure

The purified sample was flowed into an evacuated stainless steel gas cylinder; upon equilibration helium was pumped into the gas cylinder until the molecule of interest comprised 0.37% of the total pressure. Pre-photolysis signal was removed with background-subtraction, and the energy-dependent signal was normalized against the photocurrent measured by a calibrated photodiode. Two-dimensional slices of the three-dimensional data were obtained by fixing one variable (e.g., fixing reaction time at a specified m/z, observe how signal changes with respect to photon energy to retrieve the photoionization spectra). Negative ion signals indicated a depleting species, while positive signals signified species that were being formed. Primary products formed at a rate equivalent to the depletion of the reactant, whereas other chemistry products typically formed at a slower pace by comparison. The signal was integrated within the time range 0-40 ms to mitigate signal arising from other chemistry.

The absolute photoionization spectrum of 2,3-dimethylfuran was obtained by comparing the ion signal to that of a known reference compound (SI, Table S1 & Fig. S1). In this study, the reference compounds used were the calibration gases ethene, propene, and 1-butene.

The relative ion signal (S) of a molecular species at a specified photon energy (E) was directly proportional to the instrument constant (k), the mass discrimination factor (δ), the concentration (C) of the species, and the photoionization cross section at the specified photon energy ($\sigma(E)$), as indicated in Eq (1). The acquisition of the mass discrimination factor, $m^{0.643 \pm 0.086}$, was described in detail by Savee et al.,[20] where m is the molecular mass of the observed species.

$$S(E) = k\sigma(E)\delta C \quad (1)$$

By comparing the signal of the standard compound (in this case, the calibration gases) to that of the target compound, the unknown cross section was determined as a ratio of its signal intensity (S_T), photoionization cross section of the standard (σ_S), mass discrimination factor of the standard (δ_S), and concentration of the standard (C_S), to the signal intensity of the standard (S_S), mass discrimination factor of the target (δ_T), and concentration of the target (C_T), as indicated in Eq (2).

$$\sigma_T = \left(\frac{S_T(E)\sigma_S(E)\delta_S C_S}{S_S(E)\delta_T C_T}\right) \quad (2)$$

It is worth noting that the ion signal (S) and photoionization cross section (σ) are energy dependent and must be taken at the same energy for calculation consistency. For products lacking literature absolute photoionization cross sections, an estimation was made based on the semi-empirical additivity model developed by Bobeldijk et al.[21] Molar yields were used to quantify the percentage of product formed with respect to the initial reactant, 2,3-DMF. Mathematically, this is the ratio between the concentration of the product (C_P) and concentration of the reactant (C_R), as indicated in Eq (3). The resulting values were carbon-normalized by multiplying the ratio of carbons in product and reactant to achieve a 100% product yield.

$$\frac{C_P}{C_R} = \left(\frac{S_P(E)\sigma_R(E)\delta_R C_R}{S_R(E)\delta_P\sigma_P(E)}\right) \quad (3)$$

Considering the uncertainties for concentration (1%), ion signal measurements (1%), mass discrimination factor (15%), with the uncertainties for the photoionization cross section of the standard gases (10%), the uncertainties of the photoionization cross sections obtained using this mass spectrometer ranged from ±15-20%. The uncertainty of observed product ion-signal measurements varied across m/z values. Lower-abundance products generally exhibited poorer signal-to-noise

ratios, with uncertainties exceeding 20%. As a result, the uncertainties in experimental yields averaged approximately 35%.

Computational

The CBS-QB3 composite method was used to optimize the geometries of reactants, products, and transition states and to obtain accurate energies. CBS-QB3 provides a good trade-off between accuracy and computational cost, yielding heats of formation and barrier heights typically within 1-2 kcal mol^{-1} of high-level methods and experimental values.[22,23] While more recent composite schemes (e.g., G4, W1BD) and explicitly correlated coupled-cluster methods can in principle offer slightly higher accuracy, their substantially greater computational cost limits their application to systematic studies of reaction mechanisms involving numerous intermediates and transition states.[24,25] CBS-QB3 therefore remains a widely adopted choice in kinetics, combustion, and atmospheric modeling studies.

All *ab initio* quantum chemical calculations were performed using the Gaussian 09 software[26] and visualized with GaussView.[27] The uncertainty of each value obtained through the CBS-QB3 composite method was reported as ±0.05 eV (4-5 kJ/mol).[28] Triplet surface geometries were first optimized at the UB3LYP/CBSB7 level of theory, providing reliable starting structures for open-shell species at moderate computational cost. The unrestricted formulation (UB3LYP) allows α and β spin densities to differ, which is essential for correctly describing triplet electronic structures. In contrast, the restricted B3LYP formalism constrains both spin components to share the same spatial orbitals, which can lead to artificial spin pairing and inaccurate treatment of open-shell character.[29,30]

The B3LYP functional level with the 6-311G(2d,d,p) basis set was used to optimize and calculate harmonic vibrational frequencies of molecular structures.[31] Reaction pathways were confirmed using potential energy surface (PES) scans at the B3LYP/CBS7 level of theory, and optimized structures of products and transition states were calculated using CBS-QB3.[22] Intrinsic reaction coordinate (IRC) calculations were performed on optimized transition states to confirm the forward and reverse reaction pathways.[32] To confirm the possibility of intersystem crossing (ISC) between the singlet and triplet potential energy surfaces, minimum energy crossing point (MECP) calculations were carried out using the ORCA 6.1 quantum chemistry package.[33] Calculations employed the PBE0-D3BJ/def2-TZVP level of theory with TightSCF convergence and the SurfCrossOpt optimization protocol. The PBE0 functional and def2-TZVP basis set provide balanced spin-state energetics suitable for open-shell systems.[29,30,34] At the optimized MECP geometry, the residual energy splitting between the singlet and triplet surfaces is < 0.05 eV, indicating a near-degenerate crossing of the two surfaces and confirming that intersystem crossing is energetically feasible at this geometry. The energetic cost to reach the MECP from the relaxed triplet minimum was found to be within 0.5 eV, consistent with an accessible ISC pathway. Spin-orbit coupling matrix elements (SOCMEs) between the intersecting singlet and triplet states were computed at the MECP using ORCA's state-interaction spin-orbit (SI-SO) method to assess the relative efficiency of ISC at the crossing point.[33]

Following Eq (4), the adiabatic ionization energy (AIE) was obtained as the difference between the zero-point–corrected electronic energies of the molecule's ground-state neutral and cationic forms.

$$AIE = E_{0,cat} - E_{0,neu} \quad (4)$$

Where available, reference photoionization spectra were compared with experimental data to confirm product formation. In cases lacking reference spectra, simulated photoelectron spectra (PE) were generated using Franck-Condon (FC) and Franck-Condon-Herzberg-Teller methods.[35] FC overlap integrals were computed using a recursive formula by Ruhoff.[36] Integration of the PE spectrum yielded a simulated photoionization spectrum for comparison with experimental data. Agreement of both the calculated adiabatic ionization energy and simulated PI spectrum with experimental results provided strong evidence for the identification of a reaction species.

RESULTS AND DISCUSSION

The reaction of $O(^3P)$ with 2,3-DMF initiates on the triplet potential energy surface (PES) through oxygen addition to the C=C bond of the furan ring. Calculations reveal that this initial addition forms a triplet diradical complex stabilized by partial delocalization of unpaired electrons over the π-system. To provide mechanistic context for the experimental observations that follow, Scheme 1 summarizes the triplet diradical adducts (radO-2 to radO-5) and their corresponding epoxide-forming. Epoxides A and B originate primarily from direct closure across the native double bond, whereas epoxides C and D are generated after intramolecular electron-density rearrangement places spin density on the ring oxygen, enabling heteroatom-assisted ring closure following ISC. The computed MECP exhibit low energetic barriers relative to the relaxed triplet minima (< 0.5 eV), confirming that intersystem crossing is energetically feasible and enabling formation of all four epoxide intermediates (A-D), whose subsequent dissociations yield some of the observed products. In parallel with these epoxide-forming pathways, the same triplet diradicals (radO-2 to radO-5) can also undergo unimolecular dissociation directly on the triplet surface, yielding the open-chain radical intermediates that initiate the dominant product channels observed experimentally.

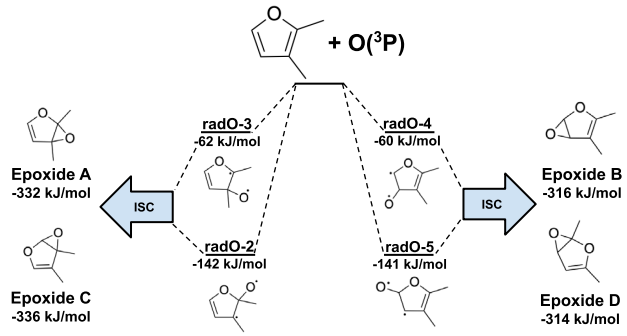

Scheme 1. Possible reaction pathways following $O(^3P)$ addition to 2,3-dimethylfuran. Energies presented are relative to that of the reactants, 2,3-DMF and $O(^3P)$.

Figure 1 depicts the mass spectrum of the reaction at 550 K, with the negative m/z 46 signal representing NO_2 and the positive m/z 30 signal representing the generation of NO and subsequently $O(^3P)$ upon successful photolysis of NO_2. Products were identified by comparing their photoionization spectra to reference or simulated spectra (see *Experimental Product*

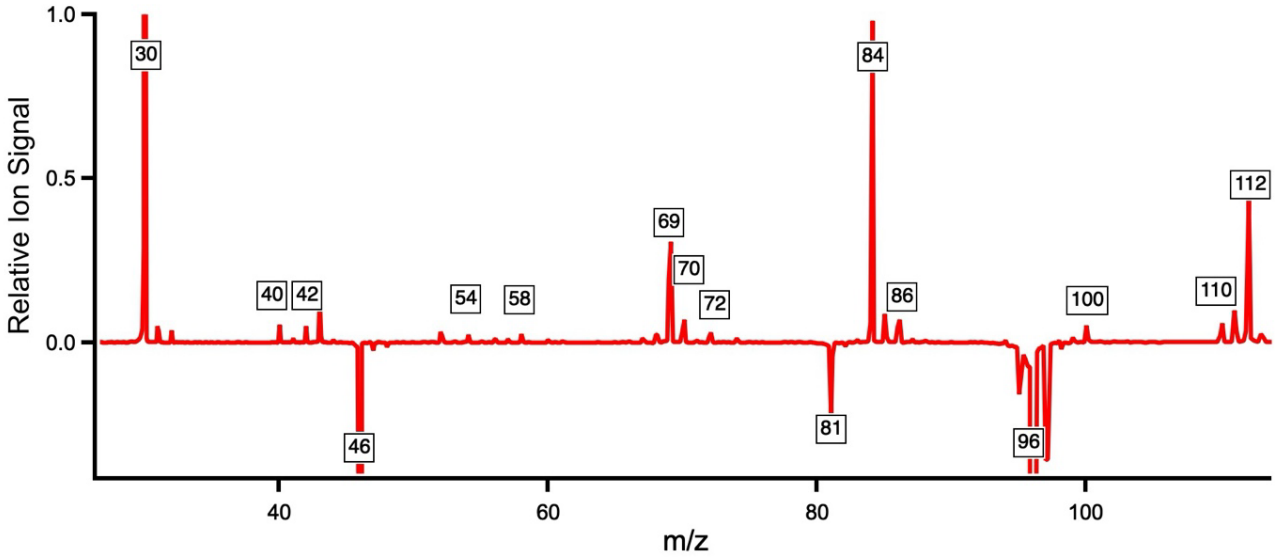

Figure 1. Mass spectrum of reactants (negative signal) and products (positive signal) at 550 K from 7.9-11 eV.

Identification section). The dominant product peak at m/z 84 is assigned to 3-methyl-3-buten-2-one, formed via loss of CO after oxygen addition.

To distinguish primary from secondary chemistry, the kinetic time traces were analyzed and compared with the inverse reactant signal (Fig. 2). This comparison is presented prior to the mass spectrum to illustrate the general kinetic behavior of detected ions The traces exhibit fluctuations of ~10–20% in the instantaneous signal intensity. At frequencies corresponding to the kinetic timescales the noise is substantially less, and because these data are used to illustrate qualitative trends and not for quantitative kinetics, this level of noise does not affect the mechanistic interpretation. Primary products generally form concurrently with the reactant decay, thus the time trace overlay with the inverse reactant signal should appear nearly identical (Fig. 2). Products coming from other chemistry generally form more slowly than primary products, so the time trace should increase at a slower rate in comparison. In contrast, the slower rise of the m/z 100 signal (dotted blue line) exemplifies secondary chemistry and is shown here solely for comparison. The signal observed at m/z 100 (dotted blue line, Fig. 1) likely originates from the reaction of $O(^3P)$ with the primary product 3-methyl-3-buten-2-one (m/z 84), forming 4-hydroxy-3-methyl-3-buten-2-one. This assignment is supported by its calculated adiabatic ionization of 8.77 eV and is included to demonstrate a typical time trace for secondary product formation reactions.

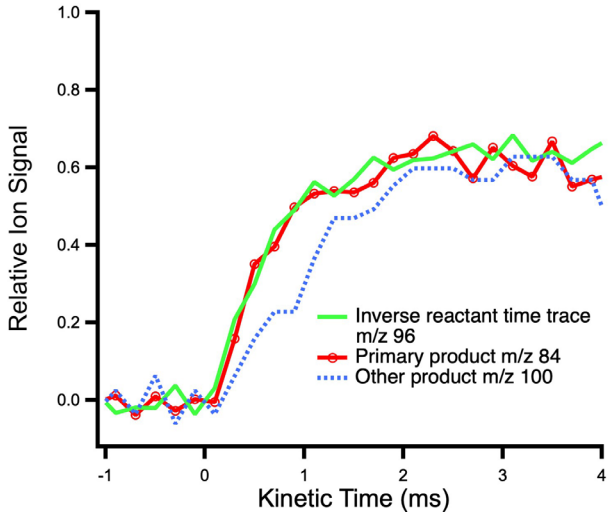

Figure 2. Time traces of a primary product (red) and other chemistry product (dashed-blue) overlayed by the inverse of the reactant time trace (time trace signal multiplied by -1), scaled for visual clarity. The reaction commences at 0 ms, when the XeF photolysis laser generates the oxidant $O(^3P)$ from NO_2.

Thermodynamic Reaction Pathways

Figure 3 depicts the singlet potential energy surface (PES) for the reaction of $O(^3P)$ with 2,3-dimethylfuran (2,3-DMF), showing the products that arise from dissociation of the four epoxide intermediates (A–D).

The brown pathway originates from epoxide B and involves C3–C4 bond cleavage through transition state T1, producing glyoxal (m/z 58) and 2-butyne (m/z 54). This reaction proceeds on the singlet surface and represents a direct fragmentation channel following epoxide opening.

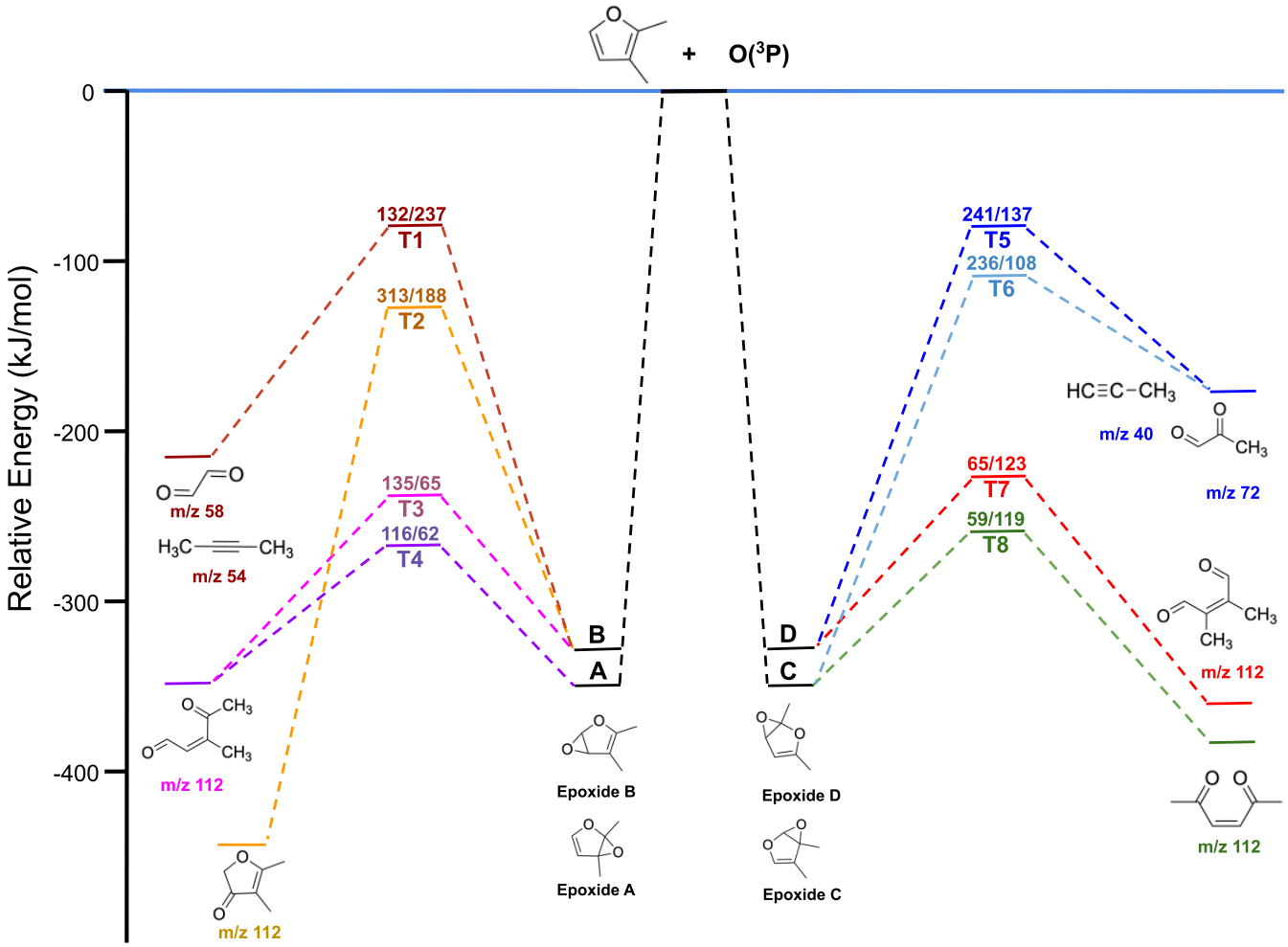

Figure 3. Computed thermodynamic pathways of products derived from epoxide intermediates A-D on the singlet potential energy surface at 0 K. Transition states are labeled as T1-T8, with energies given in kJ/mol relative to adjacent species. Atom numbering in the furan ring follows the convention O1 (oxygen) to C5 (carbon) in a clockwise direction.

The most thermodynamically favorable route from epoxide B is the orange pathway, forming 4,5-dimethyl-3(2H)-furanone (m/z 112) through an intramolecular hydrogen transfer from C4 to C5 via T2. At elevated temperatures (around 700 K), the furanone can further decompose through cleavage of the O1-C2 bond, yielding formaldehyde, carbon monoxide, and 1,2-butadiene. However, because the unimolecular dissociation barrier for this step is relatively high, the furanone is expected to remain thermally stabilized at 550 K, consistent with the absence of the m/z 54 (1,2-butadiene) signal in the experimental spectrum. Under non-thermalized conditions, species possessing excess internal energy may overcome the barrier, explaining the appearance of 1,2-butadiene in the 700 K experiment (see Figure S1 in the Supporting Information).

The kinetically preferred pathway from epoxides A and B proceeds via T3 and T4 (pink/purple pathways), with respective activation energies of 65 kJ mol-1 and 62 kJ mol-1, leading to formation of 3-methyl-4-oxo-2(Z)-pentenal (m/z 112). Both epoxides undergo an initial ring-opening step, breaking the bond between the furanic oxygen and the sp^3 carbon. The resulting unsaturated carbonyl species can then undergo C3-C4 bond rotation and cleavage, accompanied by hydrogen transfer, to yield 2-butenal (m/z 70) and ketene (m/z 42). Although accessible, this channel is non-dominant, as 3-methyl-4-oxo-2(Z)-pentenal is likely to thermalize under experimental conditions, favoring stabilization rather than further decomposition.

The blue pathways originate from epoxides C and D, which undergo cleavage of the furanic oxygen and adjacent sp^2 carbon through transition states T5 and T6, respectively. These reactions yield propyne and methylglyoxal, representing direct bond-scission channels following epoxide opening.

From epoxide D, an alternative red pathway proceeds through T7, involving cleavage between the sp^3 carbon and neighboring oxygen, to form 2Z-2,3-dimethyl-2-butenedial. This dialdehyde, structurally analogous to glutaraldehyde, is expected to be unstable in the gas phase and may require derivatization or complementary analytical techniques such as GC-MS for detection.[37] Attempts to optimize the corresponding cation using DFT (B3LYP/6-31+G(d)) in Gaussian failed to converge, suggesting that the structure is unbound and short-lived under experimental conditions.

The green pathway originates from epoxide C, in which cleavage between the furanic oxygen and the neighboring sp^3 carbon occurs via T8, producing 1,2-diacetylene. Both the products and the mechanistic features derived from epoxide C closely mirror those reported for the oxidation of 2,5-dimethylfuran with $O(^3P)$, providing additional validation for the proposed reaction scheme.[8]

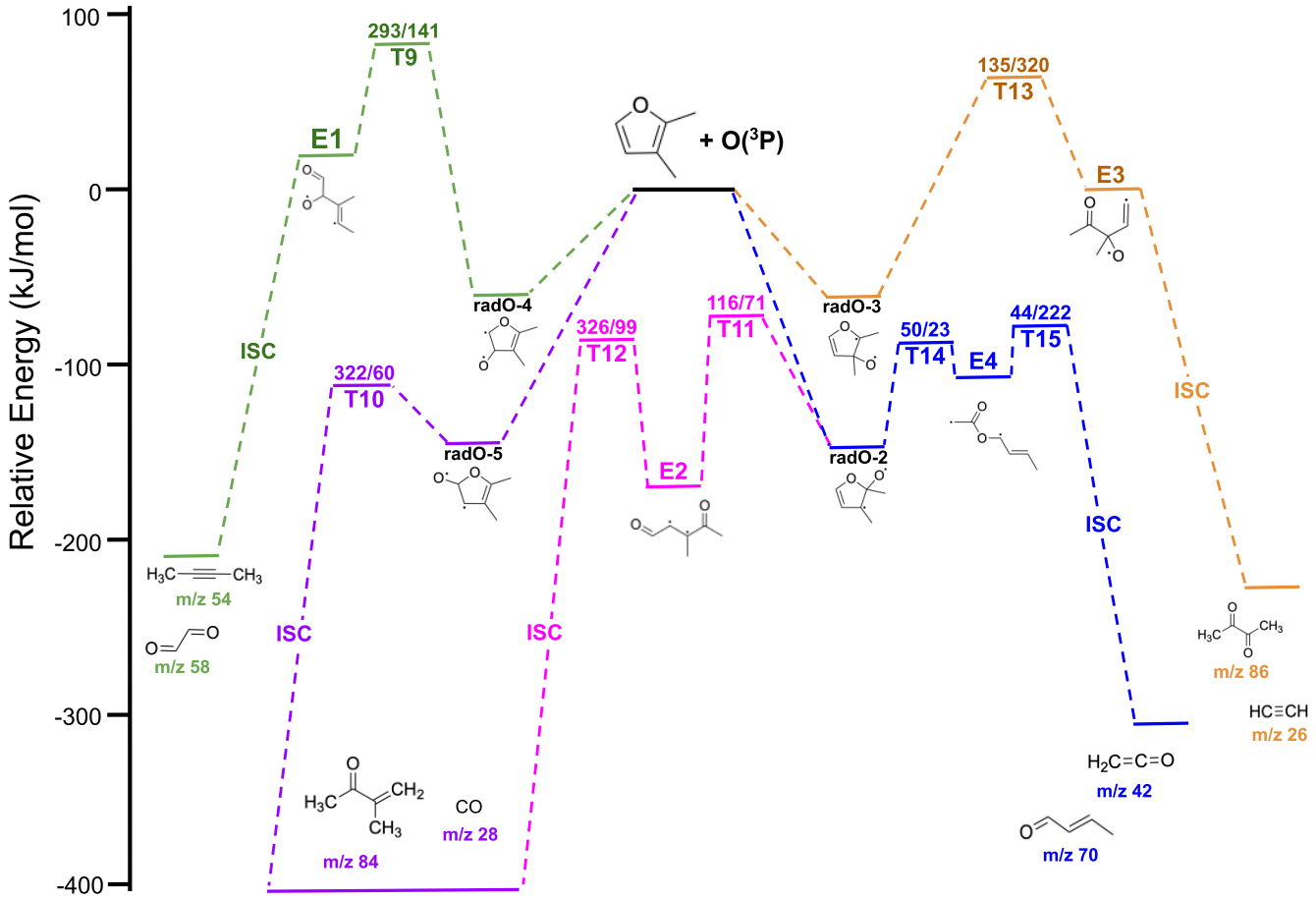

Figure 4. Triplet potential energy surface (PES) for the O(^{3}P) + 2,3-dimethylfuran reaction at 0 K showing oxygen addition to the furan ring at four distinct sites, producing diradical adducts radO-2 to radO-5 (numbering denotes the oxygen addition position). E1-E4 denote open-chain diradical intermediates formed following initial O(^{3}P) addition. Energies are given in kJ mol^{-1} relative to the adjacent species.

Figure 4 presents the triplet PES for the reaction of O(^{3}P) with 2,3-dimethylfuran, showing the initial oxygen-addition channels that form four diradical adducts (radO-2 to radO-5). The numbering corresponds to the position of oxygen addition on the furan ring. Each pathway proceeds through a distinct transition state to generate open-chain diradical intermediates (E1-E4), which undergo intersystem crossing to form the experimentally observed singlet products.

The green pathway, originating from radO-4, proceeds via T9 through cleavage of the C2-O(furan) bond to form the open-chain diradical E1, which undergoes intersystem crossing (ISC) to yield butyne (m/z 54) and glyoxal (m/z 58). This route exhibits a substantially lower transition-state barrier (141 kJ mol^{-1}) than the analogous singlet epoxide pathway (Fig.3 T1, 237 kJ mol^{-1}), indicating that the triplet surface offers a more accessible channel for C-O bond fission.

The purple pathway, originating from radO-5, corresponds to the lowest-energy barrier on the triplet surface and yields the products observed with the highest abundance. It involves an internal 1,2-hydrogen shift (C5 → C4) followed by ISC via T10 ($\Delta E^{\ddagger}$ = 60 kJ mol^{-1}) yielding 3-methyl-3-buten-2-one (m/z 84) and CO (m/z 28). At the optimized MECP, the residual singlet-triplet energy separation is only ~3 cm^{-1}, while the spin-orbit coupling matrix element (SOCME) is 6.1 cm^{-1}. Because the SOCME exceeds the S-T energy spacing, the two surfaces are strongly mixed at this geometry, indicating that intersystem crossing is energetically and electronically feasible on fast timescales.[38,39] Compared to epoxide B, where the residual singlet–triplet splitting at the MECP substantially exceeds the SOC magnitude ($\Delta E_{S\text{-}T}$ = 63 cm^{-1}, SOCME = 12 cm^{-1}), the open-chain diradical intermediates exhibit more favorable conditions for intersystem crossing due to stronger spin-orbit-induced state mixing. A parallel channel from radO-2 (pink pathway) proceeds through formation of the open-chain diradical E2 via T11, followed by a hydrogen transfer (T12, $\Delta E^{\ddagger}$ = 99 kJ mol^{-1}) to produce the same species. Both routes are among the most thermodynamically favorable on the triplet potential-energy surface, featuring comparatively low activation barriers (60-99 kJ mol^{-1}). The intense m/z 84 signal observed experimentally supports this assignment, whereas CO was not detected since its ionization threshold (13.1 eV) lies above the photon-energy range used in this study.[40]

The orange pathway, initiated from radO-3, proceeds via T13 through cleavage of the O-C4 bond of furan to form the open-chain diradical E3, which undergoes ISC to produce dimethylglyoxal and acetylene. The adiabatic ionization energy of acetylene (11.4 eV) exceeds the photon-energy range used in this experiment, hence its absence in the final mass spectrum.[40]

Finally, the blue pathway, also originating from radO-2, proceeds through C3-C4 bond cleavage (T14, 50 kJ mol^{-1}) to form the open-chain diradical E4, followed by a hydrogen transfer (T15, 44 kJ mol^{-1}) that yields ketene (m/z 42) and 2-butenal (m/z 70). This sequence represents one of the lowest-barrier triplet channels, consistent with the high relative intensity of the m/z 70 product.

Overall, the triplet potential-energy surface (PES) reveals that oxygen addition to 2,3-DMF preferentially generates open-chain diradical intermediates (E1-E4) that undergo efficient ISC and dissociate through low-barrier, exothermic channels. These features establish the triplet surface as the more favorable reaction surface and the source of the experimentally dominant product, 3-methyl-3-buten-2-one (m/z 84).

Experimental Product Identification

Figures 5 to 9 depict experimental photoionization (PI) spectra of products along with their literature or simulated PI spectra. The photolysis of nitrogen dioxide to form the reactant $O(^3P)$ generated nitrogen oxide at m/z = 30 (Fig. 5a).[41] Figure 5b depicts the PI of the product propyne at m/z = 40, matching well with the reference PI spectrum.[40] The experimental onset of 10.35 eV is a match with the literature ionization energy of 10.349 ± 0.015 eV collected from previous photoionization experiments by Cool et al.[40] and Omura et al.[42]

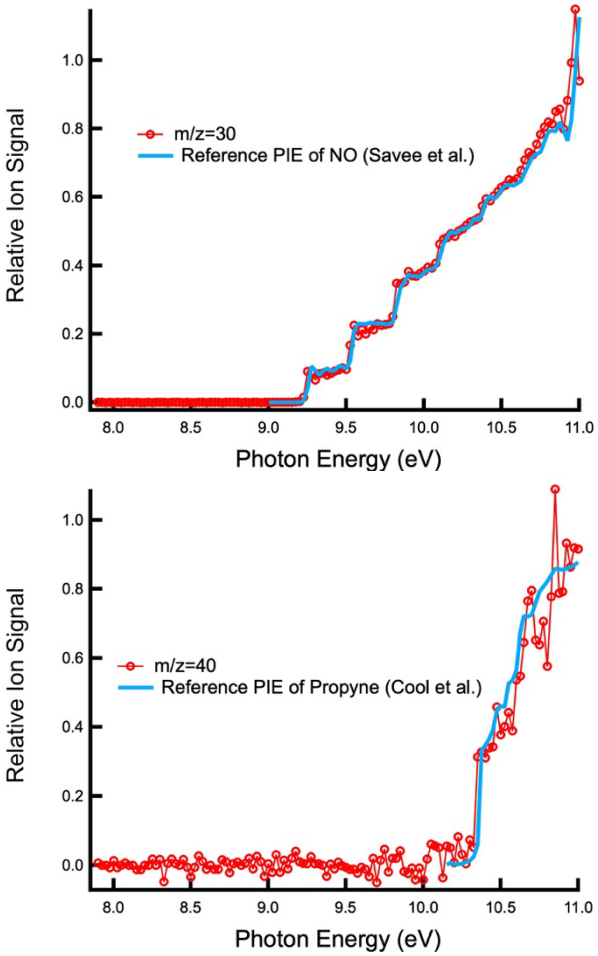

Figure 5. (a) Top: PI spectra of nitrogen oxide at m/z = 30.[20] **(b)** Bottom: PI spectra of propyne at m/z = 40.[40]

Ketene was formed at m/z = 42, matching reasonably well with the literature PI curve provided by Yang et al.'s experiments (Fig. 6a).[43] The experimental AIE of m/z 42 is approximately 9.55 eV, which is a good match with the reference PI curve's experimental value of 9.58 eV.[43] Figure 6b shows the experimental PI spectrum at m/z = 54, with the reference PI of 2-butyne superimposed.[44] The experimental AIE of 2-butyne is 9.6 eV, very close to the literature ionization energy of 9.59 ± 0.02 eV determined by Bieri et al.'s photoelectron experiments.[45]

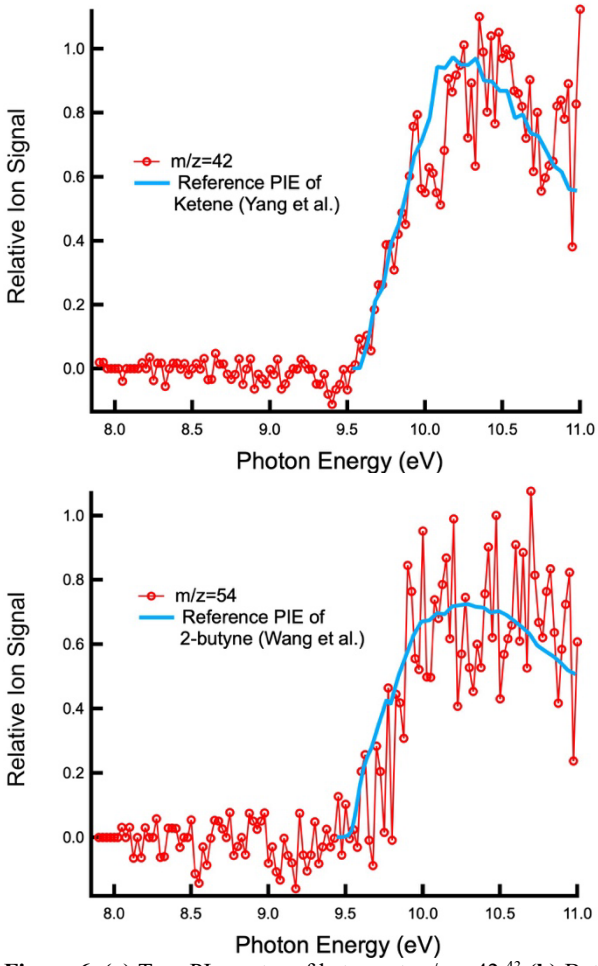

Figure 6. (a) Top: PI spectra of ketene at m/z = 42.[43] **(b)** Bottom: PI spectra of 2-butyne.[44]

Figure 7a shows the experimental PI spectrum collected for the minor product at m/z = 58, and the reference PI spectrum of glyoxal.[46] The spectra do not match well; the current experimental onset is noticeably earlier than the AIE of glyoxal at 10.2 eV, suggesting perhaps a contribution from ethenediol or the presence of a secondary product or a fragment from a product at a higher mass. Furthermore, the experimental spectrum does not match those of acetone or propenol, indicating that these compounds are unlikely to be significant contributors to the observed signal. A mechanism for formation of glyoxal is supported by thermodynamic data detailed in the following section. The signal is analyzed assuming that glyoxal is a major contributor to the observed signal; considering the poor agreement with the reference signal this is can be regarded as an upper bound. In Figure 7b, the experimental PI curve at m/z = 70 is a very good match with the reference PIE for 2-butenal.[43] Its formation is a result of the dissociation of an

intermediate on the triplet surface, also yielding ketene at m/z = 42. These products were observed in a similar oxidation experiment of 2,5-dimethylfuran with $O(^3P)$, where the formation of 2-butenal and ketene was unable to be proved.[8]

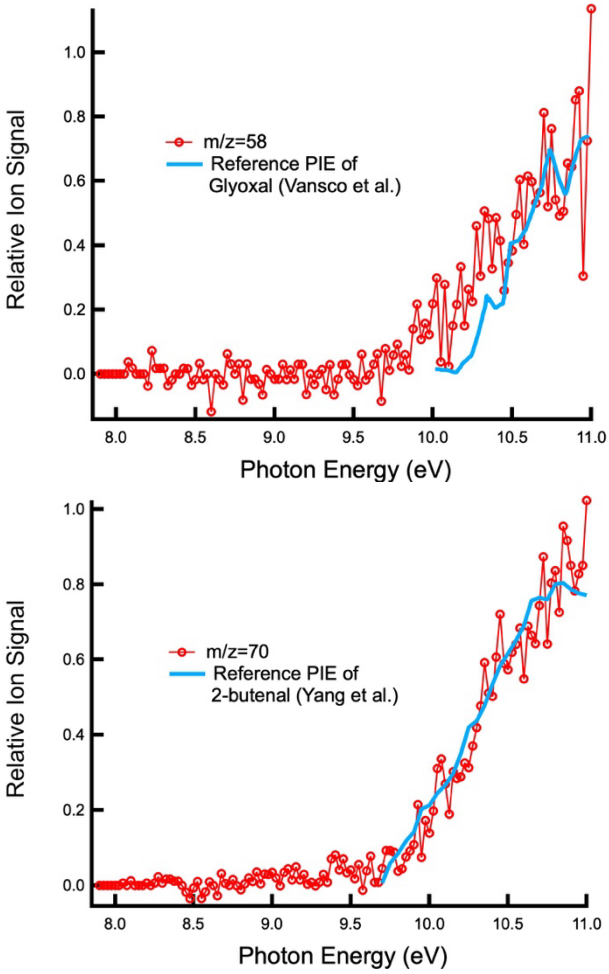

Figure 7. (a) Top: PI spectra of glyoxal at m/z = 58.[46] The experimental onset of m/z = 58 product is lower than the measured onset of glyoxal at 10.2 eV, suggesting the presence of the enol or an additional secondary product or fragment coming from a larger molecule. **(b)** Bottom: PI spectra of 2-butenal at m/z = 70.[43]

Mass 72 is the primary product methylglyoxal, shown in Figure 8a.[47] The reference PI spectrum obtained from photoionization experiments by Scheer et al. is a good match with the experimental curve.[47] Methylglyoxal's observed AIE is 9.55 eV, which is very close to the literature threshold value of 9.60 ± 0.06 eV obtained from electron impact experiments by Reed and Brand.[48] The PI spectra of 3-methyl-3-buten-2-one at m/z = 84 is presented in Figure 8b, and it is one of the primary products of the reaction (Table S2, Fig. S3). The calculated AIE of 3-methyl-3-buten-2-one is 9.52 eV, a good match with the experimental value of 9.5 eV. 3-methyl-3-buten-2-one partially dissociates upon ionization and loses a methyl group, forming a fragment at m/z 69 that is present in the experimental mass spectrum (Fig. 2).

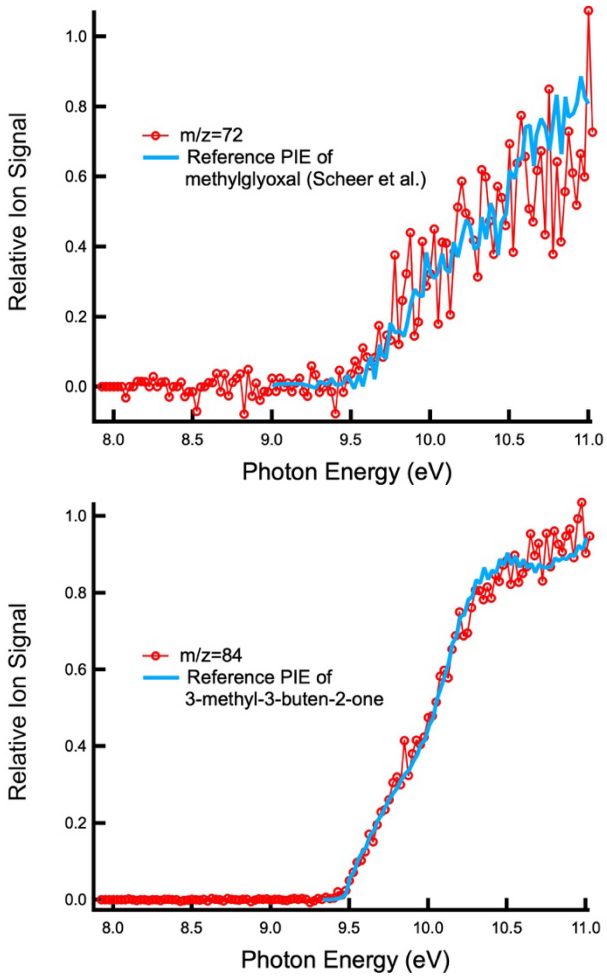

Figure 8. (a) Top: PI spectra of methylglyoxal at m/z = 72.[47] **(b)** Bottom: PI spectra of 3-methyl-3-buten-2-one at m/z = 84 (reference PI from this work, Table S1 in Supporting Information).

Figure 9a shows the PI spectra of dimethylglyoxal at m/z = 86. The reference spectra for 3-methyl-3-buten-2-one and dimethylglyoxal were experimentally determined by photoionization experiments done at the ALS, with data provided in the supplemented material (Table S3, Fig. S4). At m/z = 112, there are two primary products, 4,5-dimethyl-3(2H)-furanone and 3-methyl-4-oxo-2(Z)-pentenal. The calculated adiabatic ionization energies are 8.67 and 9.11 eV, respectively, which are a good match with the experimental values of 4,5-dimethyl-3(2H)-furanone and 3-methyl-4-oxo-2(Z)-pentenal. There is a feature that rises sharply at higher photon energy, which could correspond to the opening of a channel to an excited state of the cation. According to Koopmans' theorem, the first excited state of the 4,5-dimethyl-3(2H)-furanone ion can be estimated from the energy difference between the HOMO and HOMO-1 of the neutral species.[49] This estimate would place the first excited cation state at roughly 10.32 eV, matching the onset of the signal that rises near 10.4 eV.

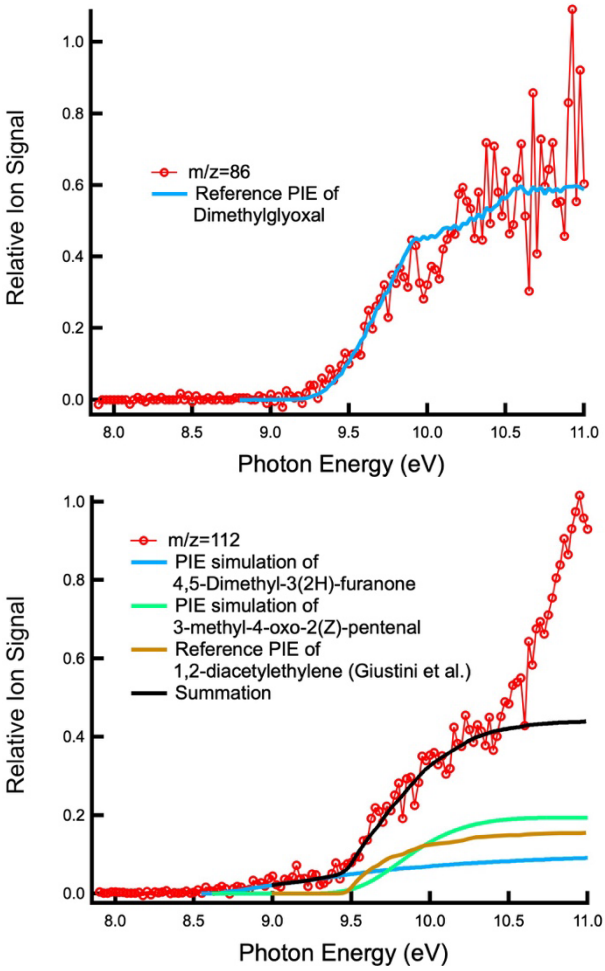

Figure 9. (a) Top: PI spectra of dimethylglyoxal at m/z = 86 (reference PI from this work, Table S2 in Supporting Information). **(b)** Bottom: PI spectrum of m/z = 112 and simulated spectra of 4,5-dimethyl-3(2H)-furanone, 3-methyl-4-oxo-2(Z)-pentenal, and 1,2-diacetylethylene.[8]

The kinetic time traces of selected products with an identified thermodynamically feasible pathway are represented in Figure 10. The reactant time trace is scaled by a factor of -0.1 for visualization purposes, and all other signals are shown unaltered, and the starting time of 0 ms marks the initiation of the reaction when the photolysis laser was turned on. The slow long-time decay in m/z 96 reflects continued consumption of 2,3-DMF by small amounts of radicals, including O-atoms, that are regenerated through secondary processes in the reaction mixture. These secondary O atoms continue to react with 2,3-DMF and sustain product formation at later times. The gradually increasing NO signal (SI, Fig. S5) supports the presence of persistent O-atoms. Products at m/z 84 and 112 show continued growth from this consumption by secondary O atoms and other radicals after the rapid initial rise from reaction of photolytically produced O atoms.

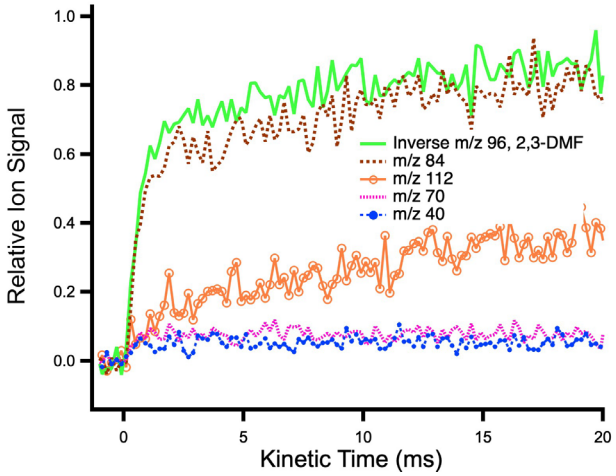

Figure 10. Kinetic time traces of products at m/z 40, 70, 84, and 112. The inverse kinetic time trace of the reactant is superimposed onto the graph in green and scaled down.

Table 1. Experimental molar yields for detected reaction products

m/z	Species	Yields and Uncertainties
40	propyne	2.6 ± 0.7%
42	ketene	2.0 ± 1.5%
54	2-butyne	0.3 ± 0.1%
58	glyoxal	1.6 ± 1.3%
70	2-butenal	7.8 ± 2.3%
72	methylglyoxal	1.5 ± 0.4%
84	3-methyl-3-buten-2-one	40 ± 10%
86	dimethylglyoxal	2.7 ± 0.7%
112	1,2-diacetylethylene	4.9 ± 1.3%
112	4,5-dimethyl-3(2H)-furanone	1.6 ± 0.4%
112	3-methyl-4-oxo-2Z-pentenal	7.1 ± 1.8%

The overall molar yields of detected products during the first 40 ms of the reaction with thermodynamically favorable pathways are reported in Table 1. Values were calculated using Eq. (3), with uncertainties obtained by error propagation. The main sources of uncertainty are ion signal fluctuations, background subtraction, limited accuracy in photoionization cross sections and mass discrimination, and small errors in pressure and flow calibration. Accounting for all products including those that were not within the detection range, the total carbon-normalized yield was 87 ± 22%. Products not within the detection range include ethyne and carbon monoxide: the abundance of ethyne and carbon monoxide was inferred based on the ratio of detected species formed from their respective reaction pathways. Although, because of the unresolved effects of secondary chemistry the yields are not identical to the branching fractions of the initial reaction, one can still draw qualitative conclusions about the relative prominence of the possible reaction pathways. 3-Methyl-3-buten-2-one is the most abundant product, comprising ~40% of all detected signal. Its formation exceeds

that of products arising from singlet-surface epoxide dissociation, which occurs on the nanosecond timescale due to the deep epoxide well (Giustini et al.) and therefore contributes far less than the biradical pathway, whose shallow well suggests a much more rapid dissociation.[8,50,51] This explains why the three m/z 112 products derived from epoxide dissociation appear at much lower abundance than the dominant m/z 84 product despite collectively forming the second-largest contribution.

Table 2. Absolute photoionization cross sections (PICS) at 11 eV obtained from literature, experimental measurements (SI, Supporting Information), and estimated calculations (Est.).

m/z	Species	Absolute PICS and Uncertainties at 11 eV (Mb)	Ref.
40	propyne	44 ± 9	[40]
42	ketene	16 ± 3	[43]
54	2-butyne	70 ± 14	[44]
58	glyoxal	10 ± 2	Est.
70	2-butenal	14 ± 3	[43]
72	methylglyoxal	16 ± 3	Est.
84	3-methyl-3-buten-2-one	22 ± 4	SI
86	dimethylglyoxal	22 ± 5	SI
112	1,2-diacetylethylene	34 ± 7	[8]
112	4,5-dimethyl-3(2H)-furanone	60 ± 12	Est.
112	3-methyl-4-oxo-2Z-pentenal	30 ± 6	Est.

The absolute photoionization cross sections of products without reported literature values (glyoxal, methylglyoxal, 4,5-dimethyl-3(2H)-furanone, and 3-methyl-4-oxo-2(Z)-pentenal) are listed in Table 2. These values were estimated using the photoionization cross section additivity model developed by Bodeldijk et al.[21] The absolute photoionization cross sections of dimethylglyoxal and 3-methyl-3-buten-2-one were experimentally determined (SI, Tables S2 & S3), while ketene, propyne, 2-butyne, 2-butenal, and 1,2-diacetylethylene have references from literature.[8,40,43–47] The photoionization cross sections of glyoxal and methylglyoxal are estimated using the experimental value for dimethylglyoxal as an upper bound, with adjustments made by subtracting the estimated contributions of one or two methyl groups at 11 eV (approximately 6 Mb per methyl group bonded to a carbon).[21] The estimated photoionization cross section of 4,5-dimethyl-3(2H)-furanone is based on the photoionization cross section of α-angelicalactone at 11 eV, 54.03 Mb, and adding the contribution of a methyl group.[15] 3-Methyl-3-buten-2-one is used as a lower-limit reference for estimating the photoionization cross section of 3-methyl-4-oxo-(2Z)-pentenal, with an additional 8.0 Mb added to account for the acetaldehyde functional group.[52]

CONCLUSION

The reaction of $O(^3P)$ with 2,3-dimethylfuran was investigated through a combined experimental and computational approach to elucidate the mechanistic origins of the observed oxidation products. The results reveal that initial oxygen addition occurs on the triplet surface, forming diradical intermediates (radO-2 to radO-5) that undergo intersystem crossing to the singlet surface. On the singlet PES, four epoxide intermediates (A-D) were identified, each dissociating through exothermic C-O and C-C bond scission pathways to yield characteristic fragments including glyoxal (m/z 58), methylglyoxal (m/z 72), and 4,5-dimethyl-3(2H)-furanone (m/z 112). The triplet PES further highlights the role of diradical dissociation leading to product formation, with several low-barrier ISC channels consistent with experimental product distributions. Major products formed on the triplet surface include 2-butenal (m/z 70), dimethyl glyoxal (m/z 86), and 3-methyl-3-buten-2-one (m/z 84), most abundant product observed. Compared to previous research on the oxidation of 2,5-dimethylfuran (2,5-DMF) with $O(^3P)$, 2,3-dimethylfuran exhibits a greater diversity of products and reaction pathways due to its molecular asymmetry, which enables multiple nonequivalent sites for oxygen addition and rearrangement. Taken together, these findings establish that $O(^3P)$ oxidation of 2,3-DMF proceeds through a coupled triplet-singlet mechanism involving both epoxidation and diradical rearrangement pathways. This mechanistic insight clarifies the reactivity of substituted furans toward atomic oxygen and provides a foundation for modeling the fate of furanic biofuel intermediates and related volatile organic compounds under atmospheric and combustion conditions.

ASSOCIATED CONTENT

Supporting Information

Absolute photoionization cross sections and spectra of the reactant 2,3-dimethylfuran and products dimethylglyoxal and 3-methyl-3-buten-2-one. Experimental photoionization curve of m/z 54 at 700 K and time trace of NO (m/z 30).

The Supporting Information is available free of charge on the ACS Publications website.

AUTHOR INFORMATION

Corresponding Author

* Department of Biological and Chemical Sciences, New York Institute of Technology, Old Westbury, NY 11568 USA
E-mail: gmeloni@nyit.edu

Present Addresses

† Department of Biological and Chemical Sciences, New York Institute of Technology, Old Westbury, NY 11568 USA
E-mail: lchen64@nyit.edu

Author Contributions

The manuscript was written through contributions of all authors. All authors have given approval to the final version of the manuscript.

ACKNOWLEDGMENT

This research used resources of the Advanced Light Source, which is a DOE Office of Science User Facility under contract no. DE-AC02-05CH11231.The participation of CAT and the operation of the multiplexed photoionization mass spectrometry machine at the Advanced Light Source was supported by the Division of Chemical Sciences, Geosciences and Biosciences, Office of Basic Energy Sciences (BES), U.S. Department of Energy (USDOE). Sandia National Laboratories is a multi-mission laboratory managed and operated by National Technology & Engineering Solutions of Sandia,

LLC (NTESS), a wholly owned subsidiary of Honeywell International Inc., for the U.S. Department of Energy's National Nuclear Security Administration (DOE/NNSA) under contract DE-NA0003525. This written work is coauthored by an employee of NTESS. The employee, not NTESS, owns the right, title and interest in and to the written work and is responsible for its contents. Any subjective views or opinions that might be expressed in the written work do not necessarily represent the views of the U.S. Government. The publisher acknowledges that the U.S. Government retains a non-exclusive, paid-up, irrevocable, world-wide license to publish or reproduce the published form of this written work or allow others to do so, for U.S. Government purposes. The DOE will provide public access to results of federally sponsored research in accordance with the DOE Public Access Plan. GM gratefully acknowledges financial support from the Institutional Support for Research and Creativity (ISRC) Grant provided by New York Institute of Technology.

ABBREVIATIONS

23DMF, 2,3-dimethylfuran; AIE, adiabatic ionization energy; FC, Franck–Condon; ISC, intersystem crossing; MECP, minimum energy crossing point; PI, photoionization; PIE, photoionization efficiency; SOCME, spin–orbit coupling matrix element.

REFERENCES

(1) Abas, N.; Kalair, A.; Khan, N. Review of Fossil Fuels and Future Energy Technologies. *Futures* **2015**, *69*, 31–49. https://doi.org/10.1016/j.futures.2015.03.003.

(2) Fazakas, E.; Neamtiu, I. A.; Gurzau, E. S. Health Effects of Air Pollutant Mixtures (Volatile Organic Compounds, Particulate Matter, Sulfur and Nitrogen Oxides) – a Review of the Literature. *Rev. Environ. Health* **2024**, *39* (3), 459–478. https://doi.org/10.1515/reveh-2022-0252.

(3) EL-Seesy, A. I.; Elshobary, M. E.; He, Z. Biofuel versus Fossil Fuel. In *Handbook of Algal Biofuels*; Elsevier, 2022; pp 181–193. https://doi.org/10.1016/B978-0-12-823764-9.00027-3.

(4) Rulli, M. C.; Bellomi, D.; Cazzoli, A.; De Carolis, G.; D'Odorico, P. The Water-Land-Food Nexus of First-Generation Biofuels. *Sci. Rep.* **2016**, *6* (1), 22521. https://doi.org/10.1038/srep22521.

(5) Naik, S. N.; Goud, V. V.; Rout, P. K.; Dalai, A. K. Production of First and Second Generation Biofuels: A Comprehensive Review. *Renew. Sustain. Energy Rev.* **2010**, *14* (2), 578–597. https://doi.org/10.1016/j.rser.2009.10.003.

(6) Patinvoh, R. J.; Taherzadeh, M. J. Fermentation Processes for Second-Generation Biofuels. In *Second and Third Generation of Feedstocks*; Elsevier, 2019; pp 241–272. https://doi.org/10.1016/B978-0-12-815162-4.00009-4.

(7) Alam, F.; Mobin, S.; Chowdhury, H. Third Generation Biofuel from Algae. *Procedia Eng.* **2015**, *105*, 763–768. https://doi.org/10.1016/j.proeng.2015.05.068.

(8) Giustini, A.; Aschi, M.; Park, H.; Meloni, G. Theoretical and Experimental Study on the O(^{3}P) + 2,5-Dimethylfuran Reaction in the Gas Phase. *Phys. Chem. Chem. Phys.* **2021**, *23* (35), 19424–19434. https://doi.org/10.1039/D1CP01724A.

(9) Zhong, S.; Daniel, R.; Xu, H.; Zhang, J.; Turner, D.; Wyszynski, M. L.; Richards, P. Combustion and Emissions of 2,5-Dimethylfuran in a Direct-Injection Spark-Ignition Engine. *Energy Fuels* **2010**, *24* (5), 2891–2899. https://doi.org/10.1021/ef901575a.

(10) Binder, J. B.; Raines, R. T. Simple Chemical Transformation of Lignocellulosic Biomass into Furans for Fuels and Chemicals. *J Am Chem Soc* **2009**, *131* (5), 1979–1985. https://doi.org/10.1021/ja808537j.

(11) Thananatthanachon, T.; Rauchfuss, T. B. Efficient Production of the Liquid Fuel 2,5-Dimethylfuran from Fructose Using Formic Acid as a Reagent. *Angew. Chem., Int. Ed.* **2010**, *49* (37), 6616–6618. https://doi.org/10.1002/anie.201002267.

(12) Zhang, Q.; Yao, M.; Luo, J.; Chen, H.; Zhang, X. Diesel Engine Combustion and Emissions of 2,5-Dimethylfuran-Diesel Blends with 2-Ethylhexyl Nitrate Addition. *Fuel* **2013**, *111*, 887–891. https://doi.org/10.1016/j.fuel.2013.04.009.

(13) Tran, L. S.; Sirjean, B.; Glaude, P.-A.; Fournet, R.; Battin-Leclerc, F. Progress in Detailed Kinetic Modeling of the Combustion of Oxygenated Components of Biofuels. *Energy* **2012**, *43* (1), 4–18. https://doi.org/10.1016/j.energy.2011.11.013.

(14) Osborn, D. L.; Zou, P.; Johnsen, H.; Hayden, C. C.; Taatjes, C. A.; Knyazev, V. D.; North, S. W.; Peterka, D. S.; Ahmed, M.; Leone, S. R. The Multiplexed Chemical Kinetic Photoionization Mass Spectrometer: A New Approach to Isomer-Resolved Chemical Kinetics. *Rev. Sci. Instrum.* **2008**, *79* (10), 104103. https://doi.org/10.1063/1.3000004.

(15) Czekner, J.; Taatjes, C. A.; Osborn, D. L.; Meloni, G. Absolute Photoionization Cross-Sections of Selected Furanic and Lactonic Potential Biofuels. *Int. J. Mass. Spectrom.* **2013**, *348*, 39–46. https://doi.org/10.1016/j.ijms.2013.04.020.

(16) Taatjes, C. A.; Osborn, D. L.; Selby, T. M.; Meloni, G.; Fan, H.; Pratt, S. T. Absolute Photoionization Cross-Section of the Methyl Radical. *J. Phys. Chem. A* **2008**, *112* (39), 9336–9343. https://doi.org/10.1021/jp8022937.

(17) Ng, M. Y.; Nelson, J.; Taatjes, C. A.; Osborn, D. L.; Meloni, G. Synchrotron Photoionization Study of Mesitylene Oxidation Initiated by Reaction with Cl(^{2}P) or O(^{3}P) Radicals. *J. Phys. Chem. A* **2014**, *118* (21), 3735–3748. https://doi.org/10.1021/jp500260f.

(18) Troe, J. Are Primary Quantum Yields of NO_2 Photolysis at $\Lambda \leq 398$ Nm Smaller than Unity? *Z. Phys. Chem.* **2000**, *214* (5), 573–581.

(19) Vandaele, A. C.; Hermans, C.; Simon, P. C.; Carleer, M.; Colin, R.; Fally, S.; Mérienne, M. F.; Jenouvrier, A.; Coquart, B. Measurements of the NO_2 Absorption Cross-Section from 42 000 Cm^{-1} to 10 000 Cm^{-1} (238–1000 Nm) at 220 K and 294 K. *J. Quant. Spectrosc. Radiat. Transf.* **1998**, *59* (3–5), 171–184. https://doi.org/10.1016/S0022-4073(97)00168-4.

(20) Savee, J. D.; Soorkia, S.; Welz, O.; Selby, T. M.; Taatjes, C. A.; Osborn, D. L. Absolute Photoionization Cross-Section of the Propargyl Radical. *J. Chem. Phys.* **2012**, *136* (13), 134307. https://doi.org/10.1063/1.3698282.

(21) Bobeldijk, M.; van der Zande, W. J.; Kistemaker, P. G. Simple Models for the Calculation of Photoionization and Electron Impact Ionization Cross Sections of Polyatomic Molecules. *Chem. Phys.* **1994**, *179* (2), 125–130. https://doi.org/10.1016/0301-0104(93)E0376-7.

(22) Montgomery, J. A.; Frisch, M. J.; Ochterski, J. W.; Petersson, G. A. A Complete Basis Set Model Chemistry. VI. Use of Density Functional Geometries and Frequencies. *J. Chem. Phys.* **1999**, *110* (6), 2822–2827. https://doi.org/10.1063/1.477924.

(23) Montgomery, J. A.; Frisch, M. J.; Ochterski, J. W.; Petersson, G. A. A Complete Basis Set Model Chemistry. VII. Use of the Minimum Population Localization Method. *J. Chem. Phys.* **2000**, *112* (15), 6532–6542. https://doi.org/10.1063/1.481224.

(24) Curtiss, L. A.; Redfern, P. C.; Raghavachari, K. Gaussian-4 Theory. *J. Chem. Phys.* **2007**, *126* (8), 084108. https://doi.org/10.1063/1.2436888.

(25) Miller, J. A.; Klippenstein, S. J. Master Equation Methods in Gas Phase Chemical Kinetics. *J. Phys. Chem. A* **2006**, *110* (36), 10528–10544. https://doi.org/10.1021/jp062693x.

(26) Frisch, M. J.; Trucks, G. W.; Schlegel, H. B.; Scuseria, G. E.; Robb, M. A.; Cheeseman, J. R. Gaussian 09. Gaussian, Inc.: Wallingford, CT **2016**.

(27) Dennington, R.; Keith, T.; Millam, J. GaussView, Version 6. Semichem Inc: Shawnee Mission, KS **2016**.

(28) Smith, A. R.; Meloni, G. Absolute Photoionization Cross Sections of Furanic Fuels: 2-ethylfuran, 2-acetylfuran and Furfural. *J. Mass Spectrom.* **2015**, *50* (11), 1206–1213. https://doi.org/10.1002/jms.3638.

(29) Adamo, C.; Barone, V. Toward Reliable Density Functional Methods without Adjustable Parameters: The PBE0 Model. *J. Chem. Phys.* **1999**, *110* (13), 6158-6170. https://doi.org/10.1063/1.478522.
(30) Grimme, S.; Ehrlich, S.; Goerigk, L. Effect of the Damping Function in Dispersion Corrected Density Functional Theory. *J. Comput. Chem.* **2011**, *32* (7), 1456-1465. https://doi.org/10.1002/jcc.21759.
(31) Balabin, R. M. Enthalpy Difference between Conformations of Normal Alkanes: Effects of Basis Set and Chain Length on Intramolecular Basis Set Superposition Error. *Mol. Phys.* **2011**, *109* (6), 943–953. https://doi.org/10.1080/00268976.2011.558858.
(32) Maeda, S.; Harabuchi, Y.; Ono, Y.; Taketsugu, T.; Morokuma, K. Intrinsic Reaction Coordinate: Calculation, Bifurcation, and Automated Search. *Int. J. Quantum. Chem.* **2015**, *115* (5), 258–269. https://doi.org/10.1002/qua.24757.
(33) Neese, F. The ORCA Program System. *Wiley Interdiscip. Rev. Comput. Mol. Sci.* **2012**, *2* (1), 73-78. https://doi.org/10.1002/wcms.81.
(34) Weigend, F.; Ahlrichs, R. Balanced Basis Sets of Split Valence, Triple Zeta Valence and Quadruple Zeta Valence Quality for H to Rn: Design and Assessment of Accuracy. *Phys. Chem. Chem. Phys.* **2005**, *7* (18), 3297. https://doi.org/10.1039/b508541a.
(35) Sharp, T. E.; Rosenstock, H. M. Franck—Condon Factors for Polyatomic Molecules. *J. Chem. Phys.* **1964**, *41* (11), 3453–3463. https://doi.org/10.1063/1.1725748.
(36) Ruhoff, P. T. Recursion Relations for Multi-Dimensional Franck-Condon Overlap Integrals. *Chem. Phys.* **1994**, *186* (2–3), 355–374. https://doi.org/10.1016/0301-0104(94)00173-1.
(37) Nagata, Y.; Ishizaki, I.; Waki, M.; Ide, Y.; Hossen, M. A.; Ohnishi, K.; Sanada, N.; Setou, M. Glutaraldehyde Fixation Method for Single-cell Lipid Analysis by Time-of-flight Secondary Ion-mass Spectrometry. *Surf. Interface Anal.* **2014**, *46* (S1), 185–188. https://doi.org/10.1002/sia.5522.
(38) Marian, C. M. Spin-Orbit Coupling and Intersystem Crossing in Molecules. *Wiley Interdiscip. Rev. Comput. Mol. Sci.* **2012**, *2* (2), 187-203. https://doi.org/10.1002/wcms.83.
(39) Pokhilko, P.; Shannon, R.; Glowacki, D.; Wang, H.; Krylov, A. I. Spin-Forbidden Channels in Reactions of Unsaturated Hydrocarbons with O(3 P). *J. Phys. Chem. A* **2019**, *123* (2), 482-491. https://doi.org/10.1021/acs.jpca.8b10225.
(40) Cool, T. A.; Wang, J.; Nakajima, K.; Taatjes, C. A.; Mcllroy, A. Photoionization Cross Sections for Reaction Intermediates in Hydrocarbon Combustion. *Int. J. Mass Spectrom.* **2005**, *247* (1–3), 18–27. https://doi.org/10.1016/j.ijms.2005.08.018.
(41) Savee, J. D.; Borkar, S.; Welz, O.; Sztáray, B.; Taatjes, C. A.; Osborn, D. L. Multiplexed Photoionization Mass Spectrometry Investigation of the O(^{3} P) + Propyne Reaction. *J. Phys. Chem. A* **2015**, *119* (28), 7388–7403. https://doi.org/10.1021/acs.jpca.5b00491.
(42) Omura, I.; Kaneko, T.; Yamada, Y.; Tanaka, K. Mass Spectrometric Studies of Photoionization. IV. Acetylene and Propyne. *J. Physical Soc. Japan* **1969**, *27* (1), 178–181. https://doi.org/10.1143/JPSJ.27.178.
(43) Yang, B.; Wang, J.; Cool, T. A.; Hansen, N.; Skeen, S.; Osborn, D. L. Absolute Photoionization Cross-Sections of Some Combustion Intermediates. *Int. J. Mass Spectrom.* **2012**, *309*, 118–128. https://doi.org/10.1016/j.ijms.2011.09.006.
(44) Wang, J.; Yang, B.; Cool, T. A.; Hansen, N.; Kasper, T. Near-Threshold Absolute Photoionization Cross-Sections of Some Reaction Intermediates in Combustion. *Int. J. Mass Spectrom.* **2008**, *269* (3), 210–220. https://doi.org/10.1016/j.ijms.2007.10.013.
(45) Bieri, G.; Burger, F.; Heilbronner, E.; Maier, J. P. Valence Ionization Energies of Hydrocarbons. *Helv. Chim. Acta.* **1977**, *60* (7), 2213–2233. https://doi.org/10.1002/hlca.19770600714.
(46) Vansco, M. F.; Caravan, R. L.; Zuraski, K.; Winiberg, F. A. F.; Au, K.; Trongsiriwat, N.; Walsh, P. J.; Osborn, D. L.; Percival, C. J.; Khan, M. A. H.; et al. Experimental Evidence of Dioxole Unimolecular Decay Pathway for Isoprene-Derived Criegee Intermediates. *J. Phys. Chem. A* **2020**, *124* (18), 3542–3554. https://doi.org/10.1021/acs.jpca.0c02138.
(47) Scheer, A. M.; Eskola, A. J.; Osborn, D. L.; Sheps, L.; Taatjes, C. A. Resonance Stabilization Effects on Ketone Autoxidation: Isomer-Specific Cyclic Ether and Ketohydroperoxide Formation in the Low-Temperature (400–625 K) Oxidation of Diethyl Ketone. *J. Phys. Chem. A* **2016**, *120* (43), 8625–8636. https://doi.org/10.1021/acs.jpca.6b07370.
(48) Reed, R. I.; Brand, J. C. D. Electron Impact Studies. Part 4.—Glyoxal, Methylglyoxal, and Diacetyl. *Trans. Faraday Soc.* **1958**, *54* (0), 478–482. https://doi.org/10.1039/TF9585400478.
(49) Tsuneda, T.; Song, J.-W.; Suzuki, S.; Hirao, K. On Koopmans' Theorem in Density Functional Theory. *J Chem Phys* **2010**, *133* (17), 174101. https://doi.org/10.1063/1.3491272.
(50) Møller, K. H.; Kurtén, T.; Bates, K. H.; Thornton, J. A.; Kjaergaard, H. G. Thermalized Epoxide Formation in the Atmosphere. *J. Phys. Chem. A* **2019**, *123* (49), 10620–10630. https://doi.org/10.1021/acs.jpca.9b09364.
(51) Miliordos, E.; Xantheas, S. S. The Origin of the Reactivity of the Criegee Intermediate: Implications for Atmospheric Particle Growth. *Angew. Chem., Int. Ed.* **2016**, *55* (3), 1015-1019. https://doi.org/10.1002/anie.201509685.
(52) Minami, T.; Ito, S.; Nakano, M. Fundamentals of Diradical-Character-Based Molecular Design for Singlet Fission. *J. Phys. Chem. Lett.* **2013**, 4 (13), 2133–2137. https://doi.org/10.1021/jz400931b

The oxidation of 2,3-dimethylfuran (2,3-DMF) by ground-state atomic oxygen O(^{3}P) was investigated using synchrotron photoionization mass spectrometry (PIMS) and CBS-QB3 calculations. Epoxide intermediates were identified, branching ratios quantified, and new low-energy oxidation pathways revealed with implications for biofuel combustion and atmospheric chemistry.